Research Square

Preprints are preliminary reports that have not undergone peer review.
They should not be considered conclusive, used to inform clinical practice,
or referenced by the media as validated information.

Gallium induces an RNR-associated nucleotide crisis and sensitizes osteosarcoma cells to cisplatin

Kristaps Klavins

kristaps.klavins_3@rtu.lv

Riga Technical University

Jingzhi Fan

Riga Technical University https://orcid.org/0000-0002-3736-0275

Annija Vaska

Riga Technical University

Xiping Jiang

Peking University

Feifei Zhou

Peking University Third Hospital

Xi Wang

Peking University

Article

Keywords: Gallium, Ribonucleotide Reductase (RNR), Metabolomics, Iron Starvation, Osteosarcoma

Posted Date: November 13th, 2026

DOI: https://doi.org/10.21203/rs.3.rs-11468521/v1

License: This work is licensed under a Creative Commons Attribution 4.0 International License.
Read Full License

Additional Declarations: There is no conflict of interest

Gallium induces an RNR-associated nucleotide crisis and sensitizes osteosarcoma cells to cisplatin

Jingzhi Fan [a,b,c,d,e], Annija Vaska [a,b], Xiping Jiang [f], Feifei Zhou [c,e*], Xi Wang [c,d*], Kristaps Klavins [a,b*]

[a]Institute of Biomaterials and Bioengineering, Faculty of Natural Sciences and Technology, Riga Technical University, Riga, Latvia

[b]Baltic Biomaterials Centre of Excellence, Headquarters at Riga Technical University, Riga, Latvia

[c]Institute of Advanced Clinical Medicine, Peking University, Beijing, China

[d]Clinical Stem Cell Research Center, Peking University Third Hospital, Beijing Advanced Center of Cellular Homeostasis and Aging-Related Diseases, Peking University, Beijing, China

[e]Department of Orthopaedics, Peking University Third Hospital, Beijing, China

[f]Department of Sports Medicine, Peking University Third Hospital, Beijing Key Laboratory of Research and Translation for Drugs and Medical Devices in Precision Diagnosis and Treatment of Sports Injuries, Institute of Sports Medicine, Peking University, Beijing, China

*Correspondence:

Feifei Zhou

zhoufeifei@pku.edu.cn

Xi Wang

xi_wang@pku.edu.cn

Kristaps Klavins

kristaps.klavins_3@rtu.lv

Abstract

Gallium (Ga) exhibits antitumor activity, but the mechanisms underlying its cytotoxicity in osteosarcoma remain incompletely defined. Here, we investigated gallium nitrate using LC–MS metabolomics, $^{13}C_2$-glutamine tracing, iron-rescue experiments, DNA synthesis and damage assays, DepMap dependency analysis, and density functional theory (DFT) modelling. In MG-63 osteosarcoma cells, gallium depleted glycolytic and pentose phosphate pathway intermediates while increasing several ribonucleotide monophosphates and nucleosides and reducing dTTP, consistent with disrupted deoxynucleotide supply. DepMap analysis revealed broad RRM1 and RRM2 dependencies in osteosarcoma models. Gallium reduced EdU incorporation, increased DNA damage detected by alkaline comet assay, and expanded the low-DNA-content/sub-G1 population without clear phase-specific arrest. Iron supplementation rescued gallium-associated loss of viability, whereas cystine, selenium, and ferrostatin-1 did not, arguing against canonical ferroptosis as the dominant death mechanism under these conditions. $^{13}C_2$-glutamine tracing showed depletion of glutamine, glutamate, and glutathione, with an increased fractional contribution of labeled glutathione driven largely by loss of the unlabeled pool. DFT cluster modelling supported the geometric feasibility of Ga accommodation within an RNR R2-like metal centre. Finally, gallium enhanced cisplatin cytotoxicity within defined

concentration ranges, and exogenous deoxynucleosides partially rescued the combination effect. Together, these findings identify an iron-dependent, RNR-associated nucleotide-metabolic vulnerability that links gallium exposure to impaired DNA synthesis and enhanced cisplatin sensitivity in osteosarcoma.

Introduction

Gallium has historically been utilized in medicine for its antibacterial properties and has recently emerged as a promising candidate for cancer therapy, demonstrating substantial anti-tumor activity across various malignancies [1–4]. Clinically, gallium-based compounds, such as KP46, have undergone preclinical testing for osteosarcoma [5] while gallium nitrate has been clinically investigated as an antineoplastic agent. Despite its growing translational potential, the fundamental mechanisms underlying gallium-induced cytotoxicity remain obscured by contradictory theories. For instance, a gallium complex featuring planar salen ligands has been reported to trigger ferroptosis [6] and numerous studies attribute gallium's cytotoxic effects primarily to reactive oxygen species (ROS) and related ferroptotic pathways [7,8]. Conversely, other investigations indicate that gallium triggers caspase-mediated apoptosis [9–11] induces cell-cycle perturbations [12], or specifically suppresses ribonucleotide reductase (RNR) and catalase activity without affecting aconitase [13].

Gallium's anticancer activity is commonly attributed to disruption of iron homeostasis. Owing to its physicochemical similarity to Fe^{3+} (ionic radii: Ga^{3+}, 0.620 Å; high-spin Fe^{3+}, 0.645 Å; Table S1), Ga^{3+} can interfere with iron transport and iron-dependent processes, including ribonucleotide reductase (RNR) activity and mitochondrial function [14]. Gallium nitrate has also been associated with increased mitochondrial ROS and induction of metallothionein and heme oxygenase-1[15]. Clinically used to treat malignancy-associated hypercalcemia, gallium nitrate has additionally been investigated as an anticancer agent. Unlike organogallium complexes, this readily dissociating salt provides a relatively simple system for studying gallium-induced cellular responses without additional organic ligands [16]. Consequently, gallium nitrate itself has been the subject of numerous clinical trials (e.g., NCT00002543, NCT00054808, NCT00002578, NCT00836173). However, how these disruptions converge on the metabolic and genomic vulnerabilities of osteosarcoma remains unclear.

To fully understand the mechanism of action for gallium and support the development of next-generation cancer treatment approaches, we utilized an in vitro osteosarcoma model treated with gallium nitrate. By deploying an interdisciplinary approach that integrates metabolomics, stable isotope tracing, and pioneering SEM-EDS elemental mapping, we aimed to map the precise metabolic bottleneck induced by gallium and visualize the competitive distribution of gallium and iron. In this context, advanced metabolomics serves as a critical bridge between analytical chemistry and tumor biology. We also used ferroptosis inhibitors to determine whether ROS accumulation drives cell death or is a secondary consequence. Ultimately, understanding these specific molecular targets provides

crucial insights into leveraging gallium as a metabolic DNA repair inhibitor, offering a rational foundation for synergistic combination therapies aimed at enhancing the activity of DNA-damaging chemotherapy.

Results

Distinct metabolic profiles between the two types of bone cells at optimized concentration

We first assessed the concentration- and time-dependent effects of gallium (Ga) on MC3T3-E1 pre-osteoblasts, NIH/3T3 fibroblasts, and MG-63, K7M2, and U2OS osteosarcoma cells over 24 and 72 h (Fig. 1A). Although sensitivity varied among cell lines and exposure times, osteosarcoma cells generally showed greater susceptibility than MC3T3-E1 cells within selected dose ranges. At 72 h, the responses of NIH/3T3 and K7M2 cells were more similar (Supplementary Fig. S1), indicating that the selectivity was context-dependent.

To examine whether these differences were accompanied by distinct metabolic responses, we profiled intracellular metabolites in MG-63 and MC3T3-E1 cells following Ga exposure (400 μM, 24 h). Z-score distributions revealed a pronounced shift toward lower relative metabolite abundances in MG-63 cells, whereas MC3T3-E1 cells showed a broader, bidirectional redistribution (Fig. 1B). These patterns suggest cell-type-dependent metabolic remodelling rather than a uniform response to Ga.

Ranked analysis of individual metabolite ΔZ values further demonstrated that the metabolic response involved multiple biochemical classes, including amino acids, organic acids, acylcarnitines and nucleotide-related metabolites (Fig. 1C). In MG-63 cells, several metabolites associated with carbohydrate and mitochondrial metabolism, including glucose 1-phosphate, acetylcarnitine, cystathionine and glutamine, were among the most strongly decreased metabolites, whereas guanosine, adenosine, AMP, CMP and several other nucleotide-related metabolites showed positive ΔZ values. MC3T3-E1 cells displayed a different metabolic response pattern, with cystine, putrescine, glucose 6-phosphate and carnitine among the metabolites showing the strongest decreases, whereas aspartic acid, CMP, glycine, lactic acid and acetyl-CoA were increased. Thus, although Ga broadly perturbed metabolism in both cell types, the direction and magnitude of individual metabolite responses differed substantially between malignant and non-malignant bone cells.

To directly identify metabolic features associated with this differential response, we compared the Ga-induced changes between MG-63 and MC3T3-E1 cells (Fig. 1D). This analysis revealed a subset of metabolites exhibiting opposing responses between the two cell types. In particular, 6-phosphogluconic acid (6-PG), argininosuccinic acid (ASA), cystathionine, histamine and several other metabolites decreased in MG-63 cells while remaining unchanged or increasing in MC3T3-E1 cells. Conversely, nucleotide-related metabolites including cytidine, GDP, GTP and AMP, together with myristoylcarnitine, showed relatively greater increases in MG-63 cells but decreases or weaker

responses in MC3T3-E1 cells. These oppositely regulated metabolites therefore represented candidate metabolic signatures distinguishing the malignant response to Ga from the adaptive response of pre-osteoblasts.

We next integrated the magnitude and direction of the inter-cell-line metabolic changes with feature-discrimination analysis to prioritize metabolites most strongly associated with the differential Ga response (Fig. 1E). Several metabolites, including cytidine, cystathionine, argininosuccinic acid and α-ketoglutarate (α-KG), emerged as prominent discriminating features. Targeted quantification further confirmed representative differential responses of α-KG, argininosuccinic acid and 6-PG between MG-63 and MC3T3-E1 cells (Fig. 1F), supporting the validity of the metabolomic screening.

Finally, pathway enrichment analysis indicated that the Ga-responsive metabolites were mainly associated with amino-acid and central carbon metabolism, including aspartate metabolism, the urea cycle, the citric acid cycle, arginine and proline metabolism, pyruvate metabolism and glycolysis-related pathways (Fig. 1G). Collectively, these findings demonstrate that Ga induces broad but fundamentally different metabolic remodelling in osteosarcoma and pre-osteoblast cells. Rather than producing a uniform metabolic suppression, Ga preferentially disrupts metabolic homeostasis in MG-63 cells while eliciting a more heterogeneous adaptive response in MC3T3-E1 cells, thereby providing a metabolic basis for the differential cellular susceptibility to Ga.

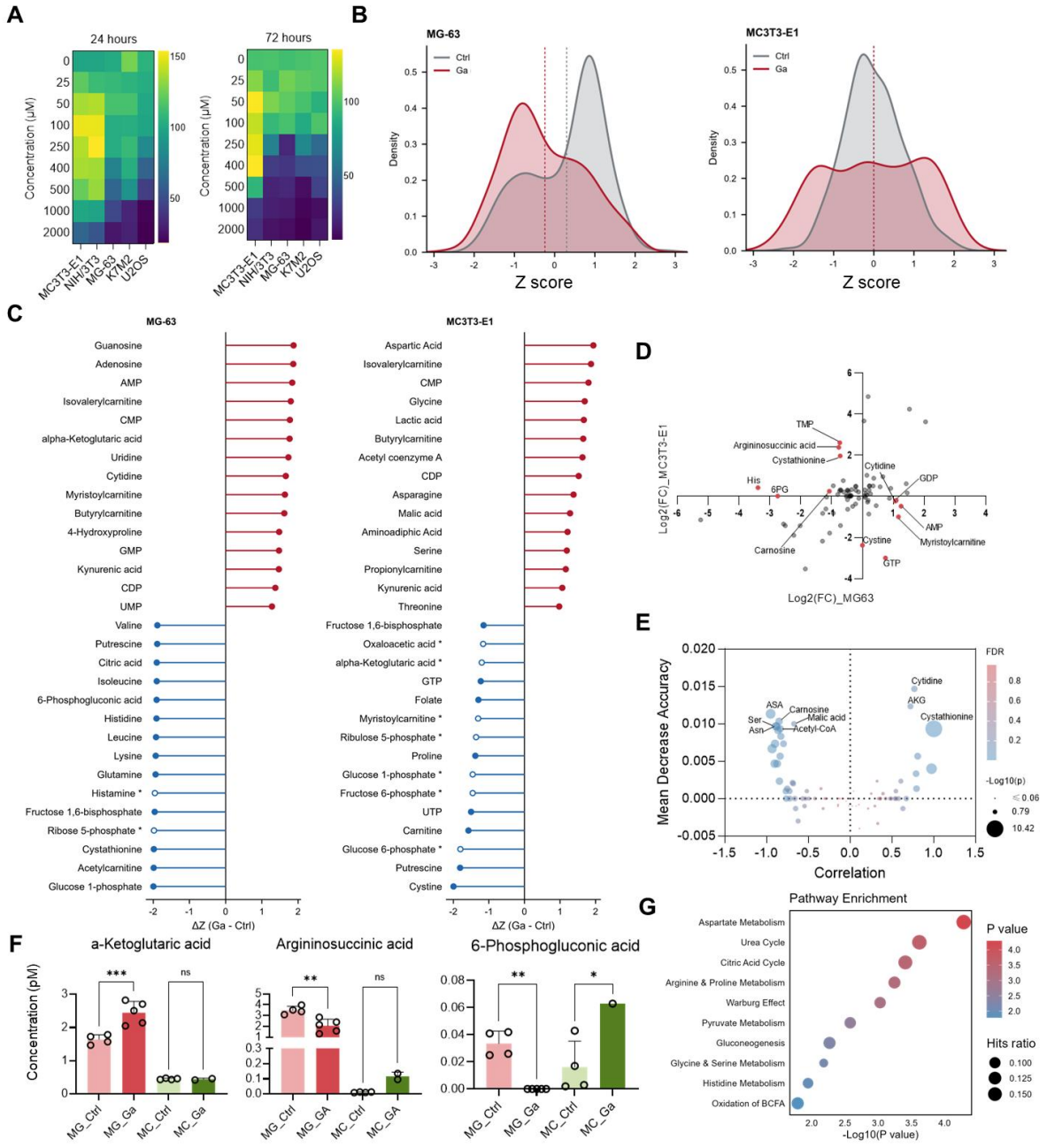


Fig. 1: Osteosarcoma and pre-osteoblast cells exhibit distinct metabolic and survival behaviors under gallium stimulation. (A) Viability of osteosarcoma (MG-63, K7M2, U2OS), pre-osteoblast (MC3T3-E1), and fibroblast (NIH/3T3) cells treated with gallium nitrate for 24 and 72 h. **(B)** Density distribution of standardized metabolite Z-scores in control and Ga-treated MG-63 and MC3T3-E1 cells (dashed lines: mean). **(C)** Ranked Ga-induced changes in metabolite Z scores ($\Delta Z = Z_{Ga} - Z_{Ctrl}$) in MG-63 and MC3T3-E1 cells. Red and blue indicate increased and decreased metabolites, respectively. Metabolites flagged during quality control because of below-detection-limit values are indicated by open symbols/asterisks. Metabolites marked with an asterisk had ≥25% of values below the detection limit, and their gallium-associated changes should be interpreted with caution. **(D)** Scatter plot comparing Ga-induced metabolite alterations ($\log_2$ FC) between MG-63 and MC3T3-E1 cells; key

inversely regulated metabolites (|Log2(FC)| >1) are highlighted. **(E)** Top discriminating metabolites prioritized by pattern search (x-axis) and Random Forest analysis (y-axis). **(F)** Metabolite levels of α-ketoglutarate, argininosuccinic acid, and 6-phosphogluconic acid. One-way ANOVA test, ***P < 0.001, **P < 0.01, *P < 0.05. Concentration was adjusted to 10^6 cells. **(G)** Pathway enrichment analysis of the inversely altered metabolites, utilizing the HMDB database. Bubble size: enrichment ratio; x-axis and colour: P-value.

Gallium disrupts cytoskeletal organization and impairs osteosarcoma cell migration

We next investigated the effects of gallium on osteosarcoma cell morphology and migration. Gallium-treated cells presented fewer filopodia than the control group. Wound-healing assays revealed significantly impaired MG-63 cell migration after 15 and 24 h of gallium exposure (Fig. 2B and Supplementary Fig. S2A). In the gelatin-coated Transwell assay, gallium reduced the CCK-8 signal from cells in the lower chamber by over 90% (Fig. 2C), potentially reflecting combined effects on migration, proliferation, and cell viability. Scanning electron microscopy (SEM) revealed substantial morphological alterations in gallium-treated cells, characterized by smoother cell surfaces and a marked reduction in filopodial extensions, while the cell membrane remained intact (Fig. 2A and Supplementary Fig. S2B, C). Consistently, confocal imaging showed pronounced F-actin disorganization, loss of perinuclear actin structures, and abnormal peripheral actin aggregation, accompanied by nuclear fragmentation (Fig. 2D). Together, these findings indicate that gallium disrupts cytoskeletal organization and impairs migration-associated cellular functions in MG-63 osteosarcoma cells.

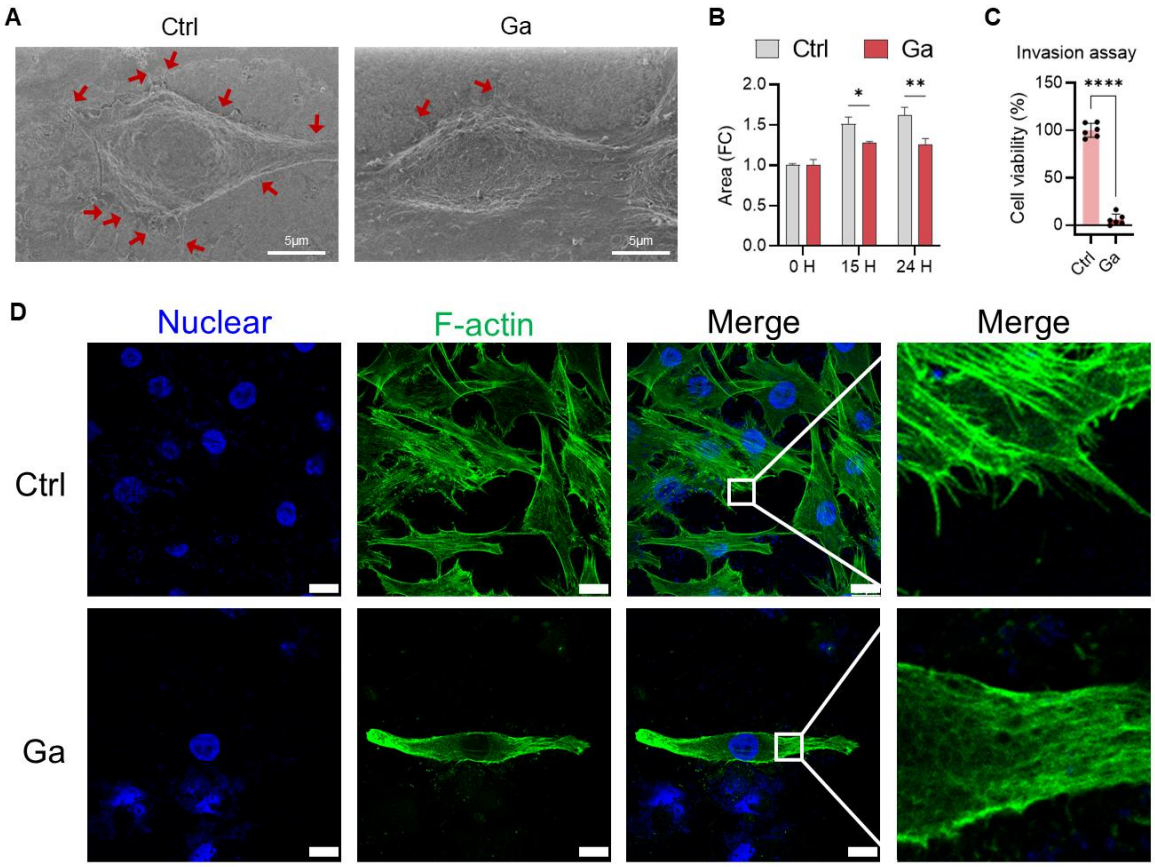


Fig. 2 Gallium disrupts the cytoskeletal structure and blocks sarcoma migration. (A) SEM image of MG-63 cells, control group and group with gallium for 24 hours. Red arrows point the filopodia. **(B)** Quantified area changes of cell migration assay. One-way ANOVA, $^{**}P < 0.01$, $^{*}P < 0.05$. **(C)** Cell viability of the lower chambers from the invasion assay after 72 hours. T-test, $^{****}P < 0.0001$. **(D)** Images of actin and nuclei. Scale bar = 2 μm.

Gallium alters energy metabolism and creates accumulation of nucleosides

We categorized the significantly altered metabolites in MG-63 cells (Fig. 3A) to map the metabolic landscape of gallium-induced toxicity. The resulting profile revealed a distinct metabolic bifurcation: while intermediates of energy production and biosynthesis—specifically within glycolysis and the pentose phosphate pathway (PPP)—were markedly downregulated, there was a simultaneous, paradoxical upregulation of nucleosides and nucleotides. Consistent with an energy crisis model, gallium treatment led to a systemic depletion of glycolytic and PPP intermediates. As modelled in Fig. 3E, we observed significant reductions in upstream metabolites such as glucose-6-phosphate (G6P) and fructose-6-phosphate (F6P), alongside critical downstream effectors like 3-phosphoglycerate (3PG). Notably, the depletion of 6-phosphogluconic acid (6-PG) and ribose-5-phosphate (R5P) confirmed the shutdown of the PPP, effectively severing the supply of NADPH for redox homeostasis and phosphoribosyl pyrophosphate (PRPP) for de novo nucleotide synthesis.

Despite the suppression of the PPP (the primary synthesis pathway), the intracellular pools of purines and pyrimidines were not depleted; rather, they massively expanded. Quantification of individual species (Fig. 3B) revealed a significant accumulation of monophosphate nucleotides—AMP, CMP, UMP, and GMP—in the gallium-treated cells. The backlog extended to their corresponding nucleosides, with adenosine, cytidine, uridine, and guanosine levels increasing by 2- to 4-fold compared to controls. The accumulation of these substrates, observed under conditions of downregulated biosynthesis (Supplementary Fig. S3), strongly suggests that downstream utilization is impaired rather than synthesis being upregulated. The critical conversion of ribonucleotides into deoxyribonucleotides is catalyzed by RNR. Consistent with the impairment of this crucial enzyme, untargeted analysis revealed a severe and significant depletion of dTTP in the gallium-treated cells (Fig. 3C). The depletion of dTTP, the accumulation of ribonucleotide-related metabolites (Fig. 3B) and the alteration of the pentose phosphate pathway suggest impaired deoxynucleotide availability and are consistent with an RNR-associated nucleotide-utilization bottleneck. The metabolites changed in the pathway are schematized in Fig. 3E.

To explore whether this vulnerability extends beyond MG-63 cells, we analyzed corrected CRISPR Chronos scores from DepMap Public 26Q1 [17]. Both RRM1 and RRM2 exhibited substantial dependency across 26 osteosarcoma models, including MG-63 (Fig. 3F). Pan-cancer analysis of 1140 models further revealed coordinated RRM1/RRM2 dependency in osteosarcoma, rather than an MG-63-specific pattern (Fig. 3G). These findings identify RNR as a broadly essential metabolic component in osteosarcoma, providing independent genetic support for the biological relevance of the observed nucleotide imbalance. We further integrated RRM2 dependency with proliferation- and iron-uptake-related features to construct an exploratory Gallium Vulnerability Index (Supplementary Fig. S4). MG-63 ranked among the more theoretically vulnerable models, although considerable heterogeneity was observed across osteosarcoma cell lines. This index remains hypothesis-generating rather than a validated predictor of gallium sensitivity. These findings suggest that gallium-induced metabolic disruption converges on impaired deoxynucleotide availability, highlighting an RNR-associated metabolic vulnerability that may contribute to osteosarcoma cytotoxicity

Metabolomic analysis of conditioned medium revealed a distinct extracellular response to gallium treatment. Among the altered metabolites, cystine decreased markedly, whereas glutamine accumulated in the medium and glutamate decreased (Fig. 3H and Supplementary Fig. S4). As the key small molecules of GSH, the changes of glutamic acid and cystine suggest that cells may have oxidative changes under the stimulation of gallium, which are worth further investigation.

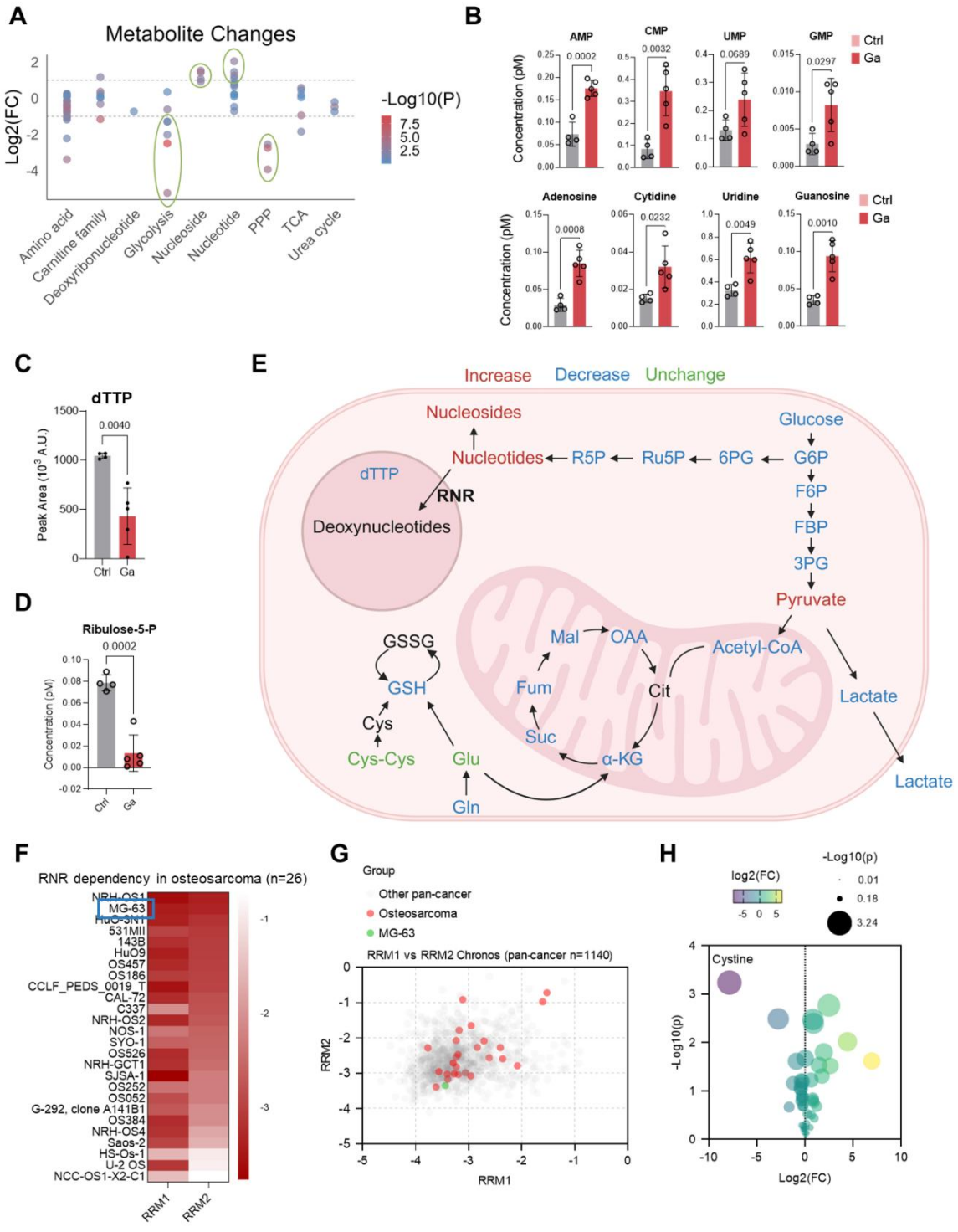


Fig. 3. Gallium disrupts central carbon metabolism and induces a ribonucleotide utilization bottleneck. (A) Fold changes of metabolites grouped by metabolic categories in Ga-treated MG-63 cells. (B–D) Quantification of nucleotides and nucleosides (B), dTTP (peak area; C), and ribulose-5-phosphate (D). Data are presented as mean ± SD (n ⩾ 4); unpaired t-test. (E) Schematic of Ga-induced metabolic alterations and the proposed RNR-associated nucleotide bottleneck. (F) Heatmap of RRM1 and RRM2 CRISPR Chronos dependency scores across 26 osteosarcoma models (DepMap Public

26Q1), with MG-63 highlighted. Lower scores indicate stronger dependency. (G) Pan-cancer comparison of RRM1 and RRM2 dependency scores across 1,140 models. Osteosarcoma models are shown in red, other cancer models in grey, and MG-63 in green. (H) Metabolomic profiling of conditioned medium from control and gallium-treated MG-63 cells presented by a volcano plot.

Iron supplementation rescues gallium cytotoxicity, whereas isotope tracing reveals selective remodelling of the glutathione pool

To investigate the role of iron in gallium-induced cytotoxicity, SEM–EDS analysis detected cellular Ga-associated signals following treatment, with both Ga and Fe signals observed after iron supplementation (Fig. 4A, B). Despite the continued presence of Ga, equimolar Fe markedly restored MG-63 cell viability at 125 and 250 μM Ga (Fig. 4C), suggesting interference with iron-dependent cellular processes. In contrast, supplementation with cystine (up to 2 mM), selenium, or ferrostatin-1 failed to improve viability (Fig. 4D–F).

We next examined glutamine-dependent antioxidant metabolism using $^{13}C_2$-glutamine tracing (Fig. 4G). Gallium reduced the measured intracellular glutamine, glutamate, and GSH pools, while iron supplementation partially preserved glutamine and glutamate but did not fully restore GSH (Fig. 4H). GSH depletion was independently confirmed by a biochemical assay. Gallium markedly depleted unlabeled M+0-GSH, whereas absolute M+2-GSH abundance remained comparable to controls (Fig. 4I). In contrast, the M+2 fractions of glutamine and glutamate remained largely unchanged (Fig. 4J), indicating reduced precursor-pool sizes without substantial changes in relative isotopic enrichment. Consequently, the M+2-GSH fraction increased from approximately 31% to 51% following Ga treatment, while iron supplementation partially restored M+0-GSH and reduced the M+2 fraction to approximately 25% (Fig. 4I, J). This pattern suggests continued but insufficient glutamine-dependent GSH renewal, with increased relative labeling primarily reflecting depletion of the unlabeled pool rather than enhanced absolute labeled GSH accumulation.

Finally, fluorescence imaging revealed increased intracellular ROS following Ga treatment, and this elevation was attenuated by iron supplementation (Fig. 4K). Together, these findings indicate that gallium induces iron-dependent redox-metabolic stress and GSH-pool remodelling, while the lack of rescue by ferroptosis-directed interventions argues against canonical ferroptosis as the predominant death mechanism under the tested conditions.

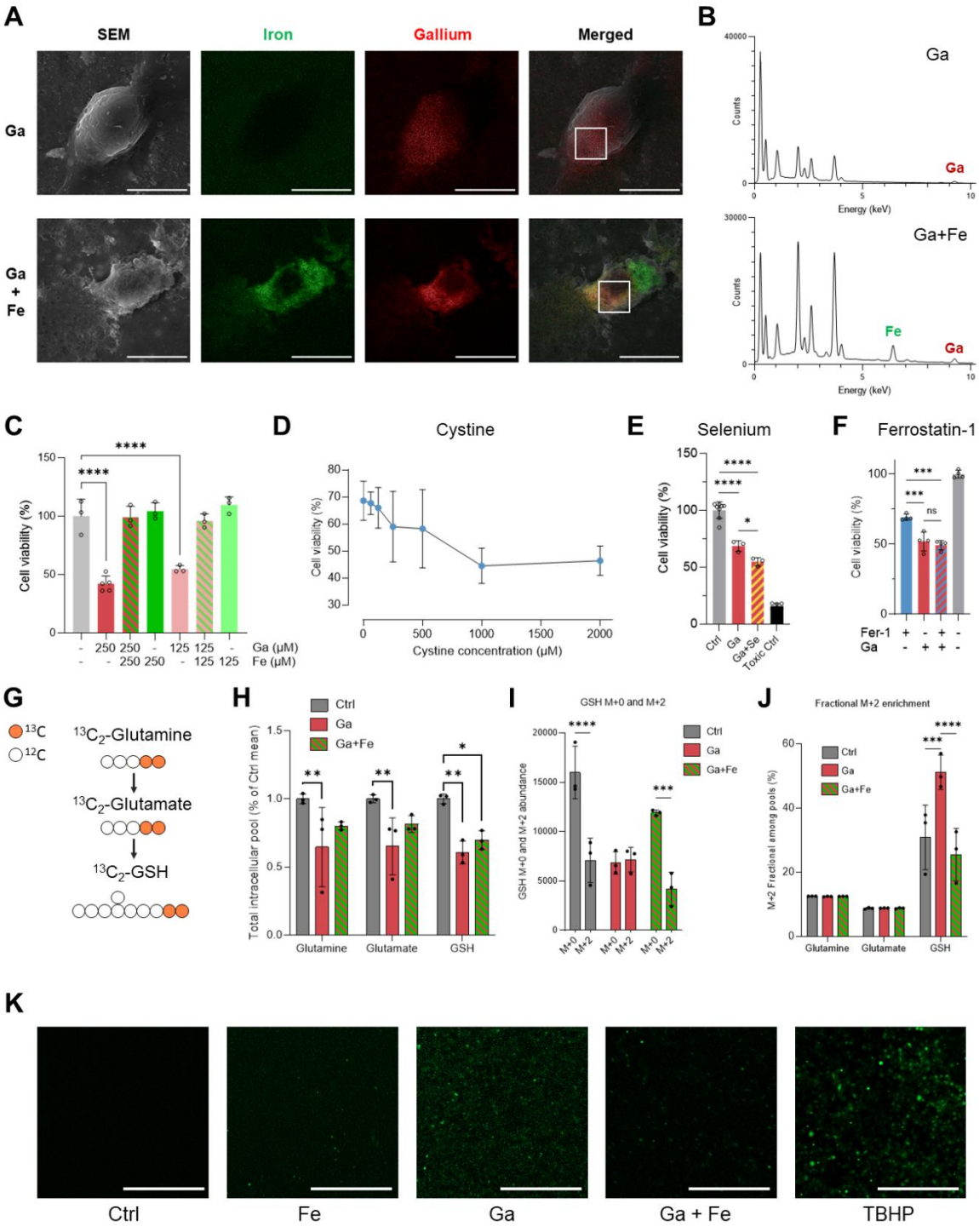


Fig. 4. Iron supplementation rescues gallium-induced cytotoxicity, whereas isotope tracing reveals glutathione-pool remodelling rather than canonical ferroptosis. (A, B) Representative SEM–EDS elemental maps **(A)** and spectra **(B)** showing cell-associated Ga (red) and Fe (green) signals in MG-63 cells. Scale bars, 10 μm. **(C)** Cell viability following Ga treatment (125–250 μM) with or without equimolar Fe supplementation. **(D–F)** Effects of cystine **(D)**, selenium **(E)**, and ferrostatin-1 **(F)** on Ga-treated cell viability. **(G)** Schematic of $^{13}C_2$-glutamine tracing. **(H)** Relative intracellular

glutamine, glutamate, and GSH pools calculated from measured M+0 and M+2 isotopologues. **(I)** Absolute abundances of M+0- and M+2-GSH isotopologues. **(J)** M+2 fractions of glutamine, glutamate, and GSH. (K) Representative intracellular ROS fluorescence images, with TBHP as a positive control. Scale bar, 100 μm. Statistical significance: ****P < 0.0001, ***P < 0.001, **P < 0.01, *P < 0.05.

Gallium suppresses DNA synthesis and alters DNA-content progression

To investigate the functional consequences of the proposed RNR-associated nucleotide bottleneck, we examined DNA damage, DNA synthesis, and cell-cycle-associated DNA content in MG-63 cells. Alkaline comet assays revealed significantly increased DNA migration and comet-tail length following gallium exposure (Fig. 5A, B). Consistently, treatment with 250 μM Ga for 24 h markedly reduced EdU incorporation, as confirmed by single-cell nuclear fluorescence quantification (Fig. 5C, D), indicating impaired DNA synthesis. PI-based DNA-content analysis revealed a significant increase in low-DNA-content/sub-G1 events, accompanied by decreased G0/G1 and G2/M fractions, whereas the S-phase fraction remained unchanged (Fig. 5E, F). These results suggest that gallium compromises DNA synthesis and genomic integrity without inducing a clearly defined phase-specific cell-cycle arrest.

To examine the structural feasibility of Ga substitution within the RNR R2 metal centre, we performed boundary-constrained r2SCAN-3c/CPCM optimizations of native FeFe and site-1 GaFe cluster models derived from mouse RNR R2 (PDB 1W68). Both models converged with similar coordination geometries. Metal–metal distances were 3.349 Å (FeFe) and 3.350 Å (GaFe), while mean metal–oxygen distances were 1.984 and 1.981 Å and mean metal–nitrogen distances were 2.129 and 2.119 Å, respectively (Fig. 5G, H). Terminal-water coordination was retained. Despite these geometric similarities, Ga exhibited near-zero local spin, whereas Fe retained high-spin character. Sequence alignment confirmed conservation of all six first-shell coordinating residues between mouse and human RRM2 (Supplementary Fig. S8). These findings support the structural feasibility of Ga accommodation within an RNR R2-like coordination environment.

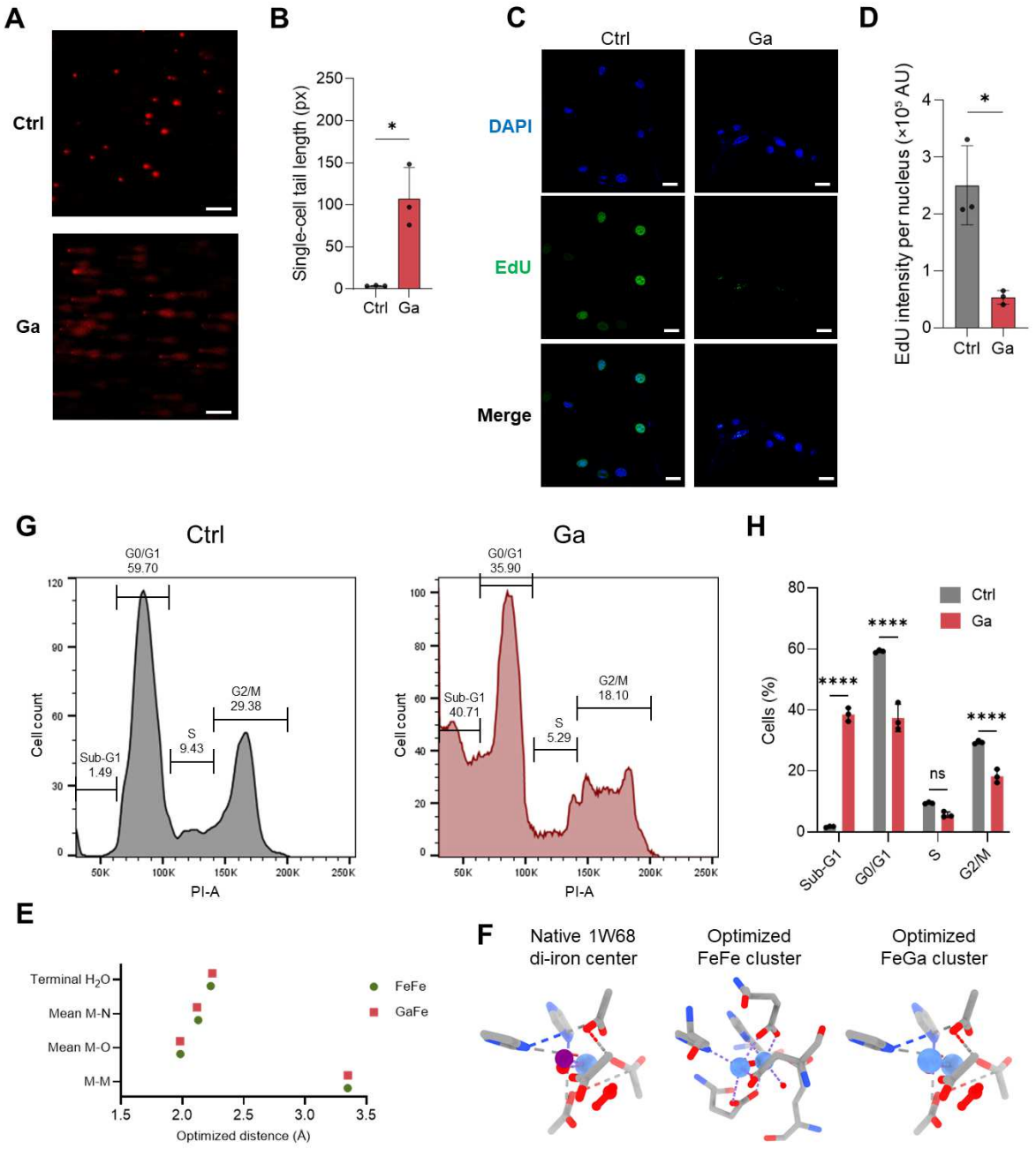


Fig. 5. Gallium impairs DNA synthesis and genomic integrity through an RNR-associated mechanism. (A) Alkaline comet-assay images of MG-63 cells under control and gallium-treated conditions, demonstrating increased DNA migration following gallium exposure. Scale bar = 30 μm. **(B)** Quantification of comet-tail length. **(C)** Representative fluorescence images of EdU incorporation in control and gallium-treated cells. Scale bar = 10 μm. **(D)** Quantification of EdU incorporation. **(E)** Representative PI-based DNA-content histograms of MG-63 cells treated with gallium and control. **(F)** Quantification of DNA-content distributions. **(G)** Comparison of structural descriptors obtained from boundary-constrained r2SCAN-3c/CPCM-optimized FeFe and GaFe RNR R2 cluster models, including the metal–metal distance, mean metal–oxygen and metal–nitrogen distances, and terminal-water coordination distance. **(H)** Native oxidized dinuclear Fe centre from mouse RNR R2 (PDB ID: 1W68)

and the corresponding optimized FeFe and site-1 GaFe cluster geometries. Ga substitution preserved the overall first-coordination-shell architecture while replacing an Fe centre with a redox-inactive metal. Structures were visualized using ChimeraX [18]. *P < 0.05; ****P < 0.0001; ns, not significant.

Gallium synergistically enhances cisplatin cytotoxicity through nucleotide limitation

Finally, we investigated whether the gallium-induced nucleotide-synthesis phenotype could be therapeutically exploited to increase sensitivity to DNA-damaging chemotherapy. A concentration matrix combining gallium and cisplatin revealed a progressive decrease in MG-63 viability with increasing exposure to either agent, while several combinations produced greater cytotoxicity than expected from the corresponding single-agent responses (Fig. 6A). This effect was particularly pronounced after 72 h, indicating that gallium potentiates cisplatin cytotoxicity within a defined concentration range.

Drug interactions were quantified using the Bliss independence model. Positive interaction regions were identified across the dose matrix, demonstrating greater-than-expected combination activity at selected concentrations (Fig. 6B). The interaction was not uniformly synergistic, suggesting a defined dose window rather than nonspecific amplification of toxicity. Additional HSA, Loewe and ZIP analyses showed model-dependent differences but identified overlapping positive-interaction regions (Supplementary Fig. S9), further supporting a genuine combination effect.

To determine whether restricted deoxynucleotide availability contributed to this response, cells treated with 100 μM Ga and 1 μM cisplatin were supplemented with a mixture of deoxyadenosine, deoxycytidine, deoxyguanosine and thymidine (Fig. 6C). Deoxynucleoside supplementation significantly increased viability at 24 h ($P < 0.001$) and 72 h ($P < 0.05$). In contrast, Fe^{3+} supplementation did not significantly rescue viability under the Ga–cisplatin condition. However, visible precipitation occurred when Ga^{3+}, cisplatin and Fe^{3+} were combined in complete medium, indicating physicochemical incompatibility that may have altered soluble drug and metal availability.

Together, the partial rescue by exogenous deoxynucleosides provides functional evidence that limited DNA-precursor availability contributes to Ga–cisplatin cytotoxicity. These findings support a dual-hit model in which gallium-associated restriction of deoxynucleotide supply compromises DNA synthesis and repair capacity, while cisplatin simultaneously increases DNA lesions, ultimately promoting genomic damage and cell death (Fig. 6D).

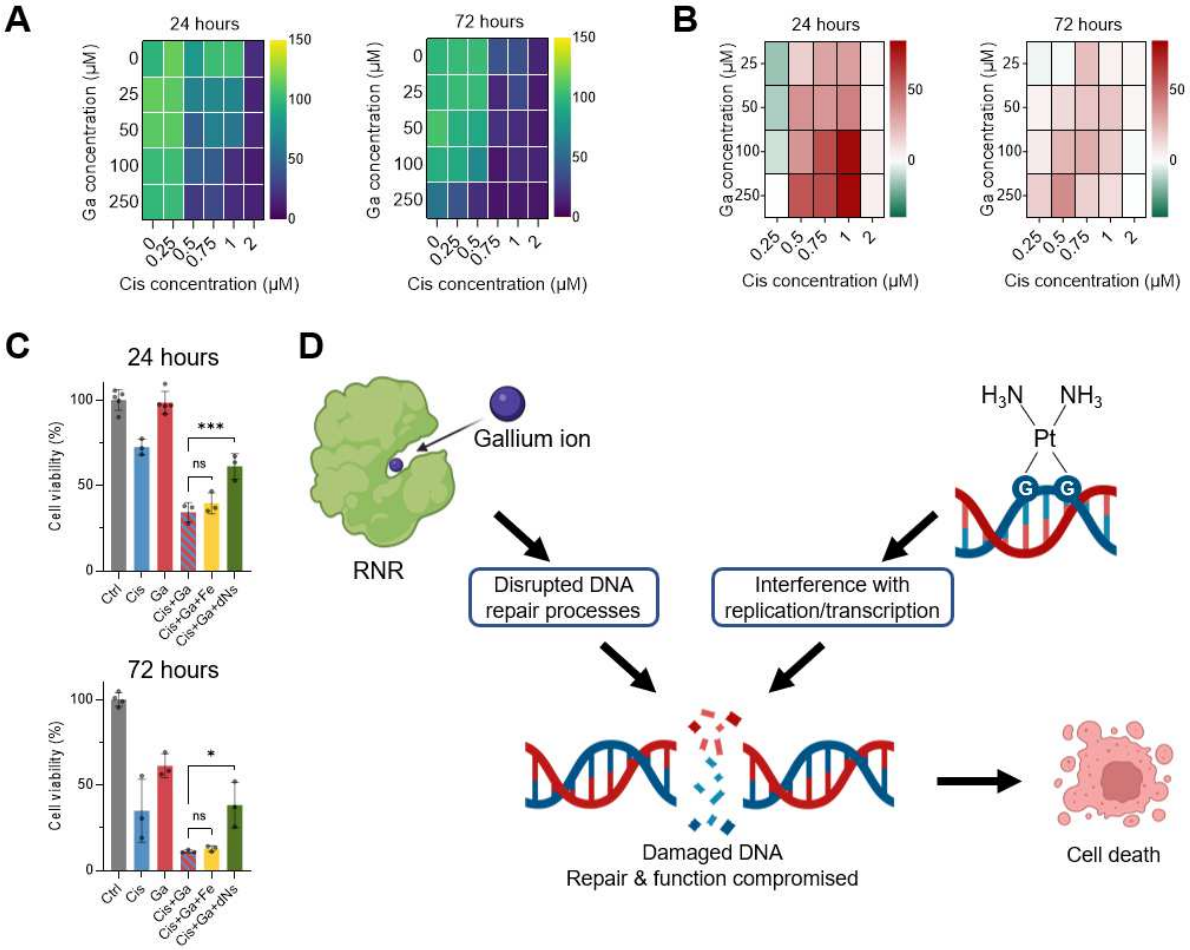


Fig. 6. Gallium potentiates cisplatin cytotoxicity across defined dose combinations. (A) CCK-8 viability matrices of MG-63 cells treated with gallium and cisplatin for 24 and 72 h, normalized to untreated controls. **(B)** Bliss interaction scores across the dose matrices; positive and negative values indicate synergy and antagonism, respectively. Additional HSA, Loewe and ZIP analyses are shown in Supplementary Fig. S9. **(C)** Effects of exogenous deoxynucleosides on gallium–cisplatin cytotoxicity. Data are presented as mean ± SD; comparisons are against the Ga + Cis group. ***P < 0.001, *P < 0.05; ns, not significant. **(D)** Proposed mechanism linking gallium-associated nucleotide limitation to enhanced cisplatin sensitivity.

Discussion

Gallium has long been viewed as an iron mimic that deprives cancer cells of essential metal-dependent functions [1,19–22]. However, its cytotoxic mechanism remains incompletely defined and is often broadly attributed to iron competition or iron deprivation [14]. Our findings suggest a more specific consequence of this deception: an iron-dependent nucleotide crisis that links central-carbon metabolism to DNA replication and chemotherapy response. While glycolytic and pentose phosphate pathway intermediates declined, ribonucleotide monophosphates and nucleosides accumulated alongside dTTP depletion. This

divergence points beyond generalized metabolic suppression toward a bottleneck in deoxynucleotide supply, with ribonucleotide reductase (RNR) emerging as a plausible mechanistic hub.

RNR is an especially attractive vulnerability, while osteosarcoma models show substantial dependence on RRM1 and RRM2 in DepMap, while EdU incorporation fell and comet-tail formation increased after gallium exposure. The expansion of the sub-G1 population, without a clear phase-specific arrest, suggests that sustained replication stress may culminate in loss of genomic integrity rather than a conventional cell-cycle checkpoint response. Our constrained DFT models add a structural dimension to this hypothesis. Ga could occupy an Fe-like coordination geometry within an R2-inspired cluster, yet lacks the local spin character of iron. This geometric mimicry and electronic mismatch suggest how gallium might interfere with metal-cofactor assembly or function [23,24].

The iron-rescue experiments reveal that this vulnerability is reversible, and that iron restored cell viability despite detectable cell-associated gallium [25]. Meanwhile, glutamine tracing exposed a distinct adaptation within the antioxidant network. Gallium depleted glutamine, glutamate and GSH, but the measured GSH M+2 pool remained comparatively stable as unlabeled GSH fell, increasing the labeled fraction. This pattern is consistent with continued glutamine-dependent GSH renewal despite declining antioxidant reserves. Reduced pentose phosphate pathway intermediates may further compromise NADPH-dependent redox buffering, potentially linking nucleotide limitation to oxidative stress. Increased ROS, together with the lack of rescue by ferroptosis-directed interventions, suggests that redox imbalance accompanies a broader metabolic crisis rather than necessarily driving canonical ferroptosis. Cytoskeletal disorganization and diminished migration could represent further manifestations of this cellular stress.

Most importantly, the nucleotide crisis offers a rationale for combining gallium with cisplatin. Earlier studies demonstrated the antitumor potential of gallium compounds in osteosarcoma [4]. Here, gallium nitrate produced positive drug interactions within defined dose ranges, and exogenous deoxynucleosides partially rescued the combination. Gallium limits nucleotide resources needed for replication and the response to DNA lesions, while cisplatin increases the burden of DNA damage. This raises the possibility that nucleotide metabolism, rather than oxidative stress alone, shapes osteosarcoma susceptibility to gallium-based combinations. Our findings position iron–nucleotide coupling as a promising therapeutic axis in gallium treatment strategy.

Conclusion

Gallium induces an iron-dependent nucleotide-metabolic crisis in osteosarcoma characterized by depletion of central-carbon intermediates, ribonucleotide accumulation, reduced dTTP, impaired DNA synthesis and DNA damage. Genetic dependency data and DFT modelling support RNR as a plausible mechanistic node, while iron rescue and the failure of ferroptosis-directed interventions indicate that

gallium toxicity is not primarily explained by canonical ferroptosis. Most importantly, gallium sensitized MG-63 cells to cisplatin, and partial rescue by exogenous deoxynucleosides provided functional evidence that restricted DNA-precursor availability contributes to this interaction. These findings identify RNR-associated nucleotide metabolism as a potential therapeutic vulnerability in osteosarcoma.

Keywords: Gallium; Ribonucleotide Reductase (RNR); Metabolomics; Iron Starvation; Osteosarcoma.

Materials and Methods

Cell culture studies

MG-63 (CRL-1427), MC3T3-E1 (CRL-2593, subclone 4), K7M2 (CRL-2836), U-2OS (CVCL_0042) and NIH/3T3 (CRL-1658, ECACC 93061524) cell lines were cultured and studied. K7M2, and MC3T3-E1 cell lines were used for fewer than 7 passages; MG-63, U-2OS and NIH/3T3 were used for fewer than 18 passages. RPMI-1640 and MEMα were used in this study because neither of these two culture medium contains added iron salts, which may be a huge factor affecting experimental results. To maintain consistent nutritional conditions for metabolomics experiments, cells were cultured in the same culture medium. To meet the growth requirements of MC3T3-E1 cells, in cell viability assay, GSH assay, and metabolomics part, cells were cultured with Minimum Essential Medium Alpha (MEMα) (Thermo Fisher) supplemented with 10% (vol/vol) Fetal Bovine Serum (FBS, Sigma-Aldrich), 1% (vol/vol), and Penicillin Streptomycin (P/S, Gibco) inside a 5% CO_2 incubator at 37 °C. RPMI-1640 (Thermo Fisher) with 10% (vol/vol) FBS and 1% (vol/vol) P/S was used as medium for fluorescent staining, iron ion intervention, invasion assay, and migration assay with MG-63 cells.

Cell viability assay

Cell viability was assessed by Cell Counting Kit-8 (Dojindo) assay. Cells were seeded at 4000 cells/well in 96-well plates with 100 μL culture medium. After 24 hours, another 100 μL culture medium with a gradient concentration of gallium nitrate (Sigma-Aldrich, ≥99.9%) was added. The final concentrations of gallium ions were 0, 25, 50, 100, 250, 400, 500, 1000, and 2000 μM, respectively. 5% DMSO was used as positive control. The assay was conducted according to the manufacturer's instructions after 24 hours and 72 hours of adding the gallium contained medium. Gallium concentrations for other experiments were adjusted according to cell density, incubation time and sub lethal functional phenotype window, based on the initial cell viability assay results.

Fluorescent staining of actin and nucleus

MG-63 cells were seeded in chamber slide (Slide 8 Well, Ibidi) overnight to attach. Medium was replaced with the gallium-contained medium (250 μM). Medium without gallium was used for control group. After 24 hours of treatment, cells were washed with PBS and then fixed for 10 min at room temperature with 4% paraformaldehyde in PBS. The fixed cells were permeabilized for 20 min at room

temperature with permeabilization buffer (0.1% Triton X-100 in PBS), followed by two washes with PBS. The cells were incubated at room temperature in the dark for 20 min with phalloidin (Alexa Fluor 488, Thermo Fisher) and DAPI (DAPI solution, Thermo Fisher) according to the manufacture's protocol. All fluorescence images were captured using a confocal microscope (STELLARIS SP8, Leica). Nuclei were excited at 405 nm, and the emission spectrum was collected in the range from 425-507 nm. Actin was excited at 497 nm, emission spectrum was collected in the range from 507-650 nm.

Cell invasion and migration assay

In the invasion assay, 6-well plates with inserts were employed. The inserts were coated with filter-sterilized gelatin derived from porcine skin (Sigma) to simulate the extracellular matrix. MG-63 cells were seeded at a density of 6×10^5 cells per well onto the gelatin-coated inserts and allowed to attach overnight. The lower chamber of the plate was filled with complete medium. Once cell attachment was established, the medium in the upper chamber (the insert) was replaced with medium lacking FBS. In the experimental groups, the medium used (both upper and lower chambers) contained gallium at a concentration of 125 μM, while the control group received medium without gallium. To quantify the migrated cells, a cell viability assay using CCK-8 was performed in the lower chamber after 72 hours [26].

In the migration assay, 12-well plates were employed. MG-63 cells were seeded at a density of 1.2×10^5 cells per well. Cells were allowed to attach overnight and, then the medium of experimental groups was changed into the medium with gallium ion (250 μM). Medium in control groups was changed into fresh medium. After 24 hours, cells were scratched with 200 μL pipette tips. Cells were washed with PBS for 3 times and changed into new medium (with or without gallium). Images were taken by microscope (C-P20, OPTIKA) at 0, 15, and 24 hours after scratching.

Intracellular metabolites collection and preparation

Both MG-63 and MC3T3-E1 cells were seeded in 24-well plates, 0.8×10^5 cells per well with 500 μL culture medium. After 24 hours, medium with gallium was added (500 μL) and the final concentration of Ga^{3+} was 400 μM. Cells were cultured for another 24 hours. Before the extraction, cell culture medium was removed, and cells were washed with ammonium bicarbonate (NH_4HCO_3, Sigma-Aldrich, ≥99.5%) solution (75 mM, 37°C). Cells were then quenched in cold 80% v/v methanol (CH_3OH, Sigma-Aldrich, ≥99.9%) and harvested by scraping. The harvested samples were centrifuged at 1000 RCF at room temperature for 5 minutes, and the supernatant was collected. The collected supernatant was dried by vacuum centrifuge. Afterward, 10 μL of the isotopically labeled internal standard mix was added to dried samples, followed by 90 μL of methanol. Reconstituted samples were transferred to glass vials and applied for liquid chromatography-mass spectrometry (LC-MS) analysis.

LC-MS based metabolomics

A Vanquish Core HPLC system (Thermo Scientific) coupled with an Orbitrap Exploris 120 (Thermo Scientific) mass spectrometer was used for the LC-MS analysis. Two chromatographic methods were employed depending on the ionization mode of mass spectrometer. The chromatographic separation was carried out on an Atlantis Premier BEH Z-HILIC Column, 1.7 µm, 2.1 * 50 mm (Waters). For the positive ionization mode the column was maintained at 40 °C, and the sample injection volume was 2 µL. The mobile phase consisted of phase A - 0.15% formic acid (v/v) in water and phase B - 0.15% formic acid (v/v) in 85% acetonitrile (v/v) with 10 mM ammonium formate. The gradient elution with a flow rate of 0.4 mL/min was performed for a total analysis time of 17 min. For the negative ionization mode the column was maintained at 40 °C, and the sample injection volume was 2 µL. The mobile phase consisted of phase A - 15 mM Ammonium bicarbonate, pH 9.00 in water and phase B - 15 mM Ammonium bicarbonate, pH 9.00 in 90% acetonitrile (v/v). The gradient elution with a flow rate of 0.4 mL/min was performed for a total analysis time of 15 min.

The Orbitrap Q Exploris 120 (Thermo Scientific) mass spectrometer was operated in either positive or negative electrospray ionization mode, spray voltage 3.5 kV, aux gas heater temperature 400 °C, capillary temperature 350 °C, aux gas flow rate 12, sheath gas flow rate 50. The metabolites of interest were analyzed using a full MS scan mode, scan range m/z 50 to 600, resolution 30000. The Trace Finder 4.1 software (Thermo Scientific) was used for data processing. A seven-point linear calibration curve with internal standardization and 1/x weighting was constructed for the quantification of the metabolites.

Bioinformatics and Dependency Analysis (DepMap)

A prespecified and reproducible analysis was performed using DepMap Public 26Q1. ModelID was used as the primary key for cross-dataset integration. Osteosarcoma, extended bone-lineage and pan-cancer cohorts were defined using OncoTree lineage metadata. The complete-case analyses displayed in the present study included 26 osteosarcoma models and 1,140 pan-cancer models. Corrected CRISPR Chronos gene-effect scores were used in their native direction, with lower values indicating stronger genetic dependency. Missing Chronos values were not mean-imputed.

Gene-level stranded RNA-sequencing values were obtained as log2(TPM+1) using entries designated as default in the DepMap release. Proliferation Score 1 was calculated as the mean standardized expression of MKI67, PCNA and MCM2–MCM7. Iron Uptake Score was calculated as the mean standardized expression of TFRC, SLC11A2 and STEAP3. RRM2 dependency strength was defined as the negative standardized RRM2 Chronos score, such that higher values indicated stronger dependency. The hypothesis-generating Gallium Vulnerability Index was calculated as the equally weighted mean of standardized RRM2 dependency strength, Proliferation Score 1 and Iron Uptake Score. Higher GVI values indicated greater theoretical vulnerability but were not interpreted as measured gallium sensitivity.

Spearman correlations, 95% bootstrap confidence intervals and Benjamini–Hochberg false-discovery-rate-adjusted P values were calculated. Core analyses used 2,000 bootstrap resamples, and drug-response analyses used 500 resamples, with random seed 20260716. Replicate screens were averaged by ModelID and compound. Basal metabolomic features were analyzed only as untreated-state characteristics and were not interpreted as gallium-induced metabolic changes.

GSH assay

MG-63 cells were seeded at 8000 cells/well in 96-well plates with 100 μL culture medium. After 24 hours, another 100 μL culture medium with gallium nitrate was added to reach the final Ga^{3+} concentration at 400 μM. After a further 24-hour incubation, cellular GSH was tested with a GSH assay kit (Merck, USA) via enzymatic cycling method according to the manufacturer's instructions. The cells were washed with PBS, followed by the addition of 200 μL Sulfosalicylic acid 5% to avoid oxidation of GSH content. Immediately afterward, the cells were lysed by placing the plate in a sonicator bath (with ice) (Cole-Parmer, USA) for 5 min. Then, all the wells were scraped and collected in a tube followed by centrifuging at 6000 rpm for 10 min. Next, 20 μL of the supernatants were collected and diluted 3 times with GSH assay buffer. Next, 20 μL of each sample was transferred to a transparent 96-well plate and mixed with a reaction mix to start the enzymatic reaction. OD was recorded using the plate reader at 450 nm at two different time points (20 min and 40 min). The results were reported as % of the control.

Stable isotope tracing with $^{13}C_2$-glutamine

MG-63 osteosarcoma cells were seeded in 12-well plates at a density of 1.0×10^5 cells per well and cultured in RPMI-1640 medium. Cells were allowed to adhere overnight before treatment. The following day, cells were treated with gallium nitrate (Ga; 250 μM), gallium nitrate in combination with iron(III) nitrate (Ga–Fe; each at 250 μM), or vehicle control. Gallium nitrate (≥99.9%) and iron(III) nitrate (≥99.95%) were purchased from Sigma-Aldrich. After 24 h of treatment, the culture medium was replaced with isotope-labeled medium consisting of RPMI-1640 supplemented with 10% fetal bovine serum and extra $^{13}C_2$-glutamine (Cambridge Isotope Laboratories). Gallium and/or iron treatment remain during this 3-hour treatment. The final total glutamine (M+0 and M+2) was 2.2 mM and the $^{13}C_2$-glutamine is 0.2 mM. This is to ensure normal cell growth without excessive glutamine accumulation, while ensuring sufficient stable isotopes for tracing. Cells were incubated in the labeled medium for 3 h to allow metabolic incorporation of the tracer. Metabolism was then quenched by rapidly washing cells with ammonium bicarbonate with a pH of 7, followed by extraction with 80% (v/v) ice-cold methanol. Cell extracts were collected and stored at −80 °C prior to mass spectrometry-based metabolomic analysis. Each experimental condition was performed in triplicate.

DNA damage assay

DNA damage was evaluated using the alkaline comet assay. MG-63 cells (6×10^5 cells/well) were cultured overnight in complete RPMI-1640 and treated with 250 μM Ga^{3+} for 24 h; untreated cells served as controls. Harvested cells were resuspended in PBS and embedded in 0.5% low-melting-point agarose on slides pre-coated with 1% normal-melting-point agarose. Slides were immersed in cold lysis buffer (2.5 M NaCl, 100 mM EDTA, 10 mM Tris, 1% Triton X-100, 10% DMSO, pH 10.0) overnight at 4°C in the dark. For DNA unwinding, slides were incubated in cold alkaline buffer (300 mM NaOH, 1 mM EDTA, pH > 13.0) for 30 min at 4°C. Electrophoresis was subsequently performed at 25 V (1 V/cm) and 300 mA for 30 min at 4°C. Finally, slides were neutralized with 0.4 M Tris-HCl (pH 7.5) for 3 × 5 min at room temperature, stained with ethidium bromide (20 μg/mL; 15585011, Thermo Scientific, MA, USA) in the dark, and visualized using a fluorescence microscope. Comet-tail length was measured using ImageJ/Fiji under identical thresholding and calibration settings.

EdU incorporation assay

DNA synthesis in MG-63 osteosarcoma cells was assessed by 5-ethynyl-2′-deoxyuridine (EdU) incorporation through EdU Proliferation Kit (iFluor 647) (ab222421). MG-63 cells were seeded in 6-well plates at 6×10^5 cells/well and allowed to attach overnight in complete RPMI-1640 medium supplemented with 10% FBS and 1% penicillin/streptomycin. Cells were then treated with gallium nitrate at a final Ga^{3+} concentration of 250 μM for 24 h, while cells maintained in gallium-free medium served as untreated controls. Following treatment, cells were incubated with EdU at a final concentration of 10 μM for 1 hour. Cells were subsequently washed with PBS, fixed with 4% paraformaldehyde, and permeabilized. Nuclei were counterstained with DAPI (DAPI solution, Thermo Fisher). Fluorescence images were acquired using identical microscope settings for all experimental groups. EdU incorporation was quantified at the single-cell level from fluorescence images using ImageJ/Fiji. Individual nuclei were identified based on DAPI staining and used as regions of interest for measurement of the corresponding EdU fluorescence signal. For each nucleus, integrated EdU fluorescence intensity was measured and corrected for local background fluorescence. Identical image-acquisition and analysis settings were applied to all experimental groups. Multiple cells from randomly selected fields were quantified for each condition, and corrected EdU fluorescence intensity was expressed in arbitrary units (AU) using ImageJ/Fiji.

Cell-cycle analysis

MG-63 cells were seeded in 6-well plates at a density of 6×10^5 cells per well and allowed to attach overnight in complete RPMI-1640 medium supplemented with 10% FBS and 1% penicillin/streptomycin. Cells were subsequently treated with gallium nitrate at a final Ga^{3+} concentration of 250 μM for 24 h, while cells maintained in gallium-free medium served as untreated controls. Following treatment, both adherent and detached cells were collected to avoid selective loss of damaged or low-DNA-content cells. Cells were washed twice with ice-cold PBS and fixed in 70%

ethanol at 4 °C overnight. Fixed cells were washed with PBS, incubated with RNase A to remove cellular RNA, and stained with propidium iodide at room temperature in the dark. Flow cytometry was performed using a BD Biosciences FACSAria II. DNA-content histograms were analyzed using FlowJo version 10.8.1, and the relative proportions of low-DNA-content/sub-G1, G0/G1, S-phase and G2/M-associated populations were determined using identical analysis settings for control and gallium-treated samples.

Gallium–cisplatin combination viability matrix

MG-63 cells were seeded at 4000 cells per well in 96-well plates containing 100 μL of complete RPMI-1640 medium and allowed to attach for 24 h, using the same seeding conditions as in the single-agent viability assay. Gallium nitrate and cisplatin were prepared in complete culture medium and combined in a concentration matrix. The final gallium concentrations were 0, 25, 50, 100 and 250 μM, and the final cisplatin concentrations were 0, 0.25, 0.5, 1 and 2 μM. An additional 100 μL of two-fold concentrated drug-containing medium was added to each well to obtain the indicated final concentrations in a total volume of 200 μL.

Cell viability was measured after 24 and 72 h of drug exposure using the Cell Counting Kit-8 (CCK-8; Dojindo) according to the manufacturer's instructions, using the same assay conditions as described for the single-agent gallium viability experiments. Viability was normalized to untreated control cells at the corresponding time point and expressed as percentage of control. Drug interactions were quantified from the gallium–cisplatin concentration matrices using four complementary reference models: Bliss independence, highest single agent (HSA), Loewe additivity and zero interaction potency (ZIP). Cell viability values were normalized to untreated controls at the corresponding time point and converted to fractional inhibition before interaction analysis. Interaction scores were calculated for all non-zero gallium–cisplatin dose combinations. Positive interaction scores indicate greater-than-expected combination activity, values close to zero indicate an approximately additive interaction, and negative scores indicate antagonism under the corresponding reference model.

Deoxynucleoside and iron rescue of gallium–cisplatin cytotoxicity

MG-63 osteosarcoma cells were seeded in 96-well plates at 4,000 cells per well and allowed to attach for 24 h in complete RPMI-1640 medium supplemented with 10% FBS and 1% penicillin/streptomycin. Cells were subsequently treated with gallium nitrate (Ga; 100 μM), cisplatin (Cis; 1 μM), or their combination. To determine whether exogenous nucleotide precursors could alleviate the cytotoxicity induced by combined Ga and cisplatin treatment, a deoxynucleoside mixture (dNs, Aladdin) consisting of 2′-deoxyadenosine, 2′-deoxycytidine, 2′-deoxyguanosine and thymidine was added at a final concentration of 10 μM each. In parallel, iron rescue was examined by supplementation with iron(III) nitrate at a final Fe^{3+} concentration of 100 μM. The experimental groups included untreated control, Cis alone, Ga alone, Ga + Cis, Ga + Cis + Fe, and Ga + Cis + dNs. Cell viability was assessed after 24 and

72 h of treatment using the CCK-8 (Dojindo) according to the manufacturer's instructions. Viability was normalized to the untreated control at the corresponding time point and expressed as percentage of control. For statistical evaluation of the rescue effect, each time point was analyzed independently by one-way ANOVA followed by Dunnett's multiple-comparison test, using the Ga + Cis group as the reference for comparisons with the Ga + Cis + Fe and Ga + Cis + dNs groups.

Intervention of iron ions

To modify the complete medium, gallium nitrate and/or iron (III) nitrate (Sigma-Aldrich, ⩾99.95%) were added and filter sterilized. The final concentration of gallium ions and/or iron ions used was 125 μM and 250 μM, respectively. MG-63 cells were seeded at a density of 8000 cells per well in 96-well plates with an initial volume of 100 μL of the original culture medium. After 24 hours, the medium was aspirated and replaced with medium supplemented with the respective/mixed metal ions. Cell viability was assessed using the CCK-8 assay after a further 24-hour incubation period.

Intracellular ROS evaluation

Intracellular ROS levels were assessed using the DCFDA/H2DCFDA Cellular ROS Assay Kit (Abcam) according to the manufacturer's protocol. MG-63 osteosarcoma cells were seeded in 96-well plates (1×10^4 cells/well) and allowed to attach overnight. Cells were washed with PBS and incubated with 20 μM DCFDA for 40 min at 37°C in the dark, followed by gentle washing with assay buffer. Fluorescent dye–loaded cells were then treated with gallium nitrate (400 μM), iron (III) nitrate (400 μM), their combination (400 μM each), or TBHP (110 μM; positive control), while untreated cells served as a negative control; all treatments were prepared in supplied buffer. After 4 hours of incubation at 37°C, fluorescence was visualized using an inverted fluorescence microscope (LSM 900, Zeiss).

Constrained DFT cluster modelling of the RNR R2 dinuclear metal centre

The oxidized dinuclear iron centre of mouse ribonucleotide reductase R2 (PDB ID: 1W68) was used as the structural template because it contains a fully occupied Fe–Fe centre, whereas the human RRM2 structures 2UW2 and 3OLJ do not provide an equivalently complete crystallographic dinuclear cofactor. A 52-atom cluster was constructed from the two metal sites, the bridging oxo ligand, terminal coordinating water, and methyl-capped side-chain fragments of Asp139, Glu170, His173, Glu233, Glu267 and His270. Two models were examined: the native diferric FeFe model and a mixed GaFe model in which site 1 Fe was replaced by Ga while site 2 remained Fe. The μ-oxo/terminal-H2O protonation pattern and cluster composition were held consistent between models. Boundary carbon atoms introduced by side-chain truncation were constrained, whereas the two metals, first-shell donor atoms, bridging oxo and terminal water were allowed to relax.

Geometry optimizations were performed with ORCA using r2SCAN-3c, TightSCF and TightOpt with a conductor-like polarizable continuum model representing a protein-like dielectric environment

(epsilon = 4.0). The FeFe model was initialized as an antiferromagnetically coupled broken-symmetry diferric state, and the GaFe model was treated with a high-spin Fe(III) centre and closed-shell Ga(III). Normal termination and geometry convergence were verified from the ORCA output. Metal–metal, individual metal–donor and terminal-water distances were calculated from the final optimized coordinates. Mulliken and Löwdin spin populations and the reported $<S^2>$ values were extracted from the converged electronic structures. To evaluate the structural feasibility and local electronic states, analyses focused on the optimized coordination geometries, metal–donor distances, and local spin populations of the constrained cluster models, rather than thermodynamic substitution free energies. Sequence conservation of the first-shell metal-coordinating residues was assessed by aligning the reviewed canonical mouse Rrm2 and human RRM2 sequences and mapping the 1W68 structural residue numbering to the corresponding UniProt sequences. Human RRM2 structures 2UW2 and 3OLJ were used as additional residue-numbering references.

Ionic-radius-guided coordination geometry screening

The crystallographic structure of mouse RNR R2 containing a complete oxidized dinuclear iron cluster (PDB ID: 1W68) was used as a structural template for preliminary metal-site compatibility analysis. Human RRM2 structures 2UW2 and 3OLJ were used as human-sequence references; 2UW2 contains a single crystallographically resolved Fe(III) ion, whereas 3OLJ does not contain a modelled iron cofactor. The crystallographic Fe coordinates in 1W68 were replaced by Ga^{3+} or selected control ions without altering the initial metal positions. First-shell ligand atoms were subsequently adjusted toward ion-specific target distances estimated from six-coordinate Shannon ionic radii and donor-atom radii, while the protein backbone and ligand identities were retained. Average metal–oxygen and metal–nitrogen distances and the displacement of first-shell ligand atoms relative to the native Fe-containing structure were calculated. This rigid geometric screening served as an initial structural assessment to evaluate steric accommodation and first-shell coordination compatibility upon Ga^{3+} substitution, based on empirical Shannon ionic radii.

Statistical analysis

All cell experiments were performed at least triplicate. The data are expressed as mean ± SD. The metabolite profiles were analyzed by MetaboAnalyst 5.0 and GraphPad Prism 9. Metabolomics data was normalized by log transformation (base 10) and auto scaling (mean-centered and divided by the standard deviation of each variable) in MetaboAnalyst 5.0 [27]. For each metabolite, values reported as below the limit of detection (<LOD) or equal to zero were replaced with one half of the smallest positive value observed for that metabolite, log2-transformed, and then standardised to a Z score as $z = (x - \mu) / \sigma$, where μ and σ are the mean and population standard deviation across all samples of the given cell line. MG-63 and MC3T3-E1 samples were standardised independently, so Z scores are not directly comparable in absolute magnitude between the two cell lines; the gallium-associated change for each metabolite was expressed as ΔZ (mean Z of Ga-treated samples minus mean Z of control samples).

One-way ANOVA test was applied with multiple comparisons, comparing the mean of each group with the mean of every other group. Differences were analyzed by two-sided t-test. Pathway analysis and enrichment analysis used The Small Molecule Pathway Database as the pathway library. Visualization of the enrichment network of metabolites correlation was performed by Metscape 2 in Cytoscape 3.9.1.

To isolate metabolites that exhibit cell-type-dependent responses to Gallium, we developed a fold-change-based classification workflow (Fig. 1E). First, raw metabolite intensities were normalized. For each of the four biological replicates (n = 4) in the Gallium-treated groups (MG-63 and MC3T3-E1), a Fold change value was calculated relative to the average intensity of the corresponding untreated control group. This transformation generated a normalized dataset consisting of 8 data points per metabolite (4 fold change values for MG-63 and 4-fold change values for MC3T3-E1). This dataset served as the input for two parallel analyses, Random Forest classification to distinguish between the two cell types based on their metabolic fold change profiles and pattern search (correlation analysis) to identify metabolites with high importance and strong inverse correlation.

Abbreviations

6-PG: 6-phosphogluconic acid

3PG: 3-phosphoglycerate

ASA: argininosuccinic acid

BBCE: Baltic Biomaterials Centre of Excellence

CCK-8: Cell Counting Kit-8

Cis: cisplatin

F6P: fructose-6-phosphate

FBS: Fetal Bovine Serum

FC: fold change

Fer-1: ferrostatin-1

G6P: glucose-6-phosphate

GSH: glutathione

LC-MS: liquid chromatography-mass spectrometry

MEMα: Minimum Essential Medium Alpha

P/S: Penicillin Streptomycin

PDB: Protein Data Bank

PPP: pentose phosphate pathway

PRPP: phosphoribosyl pyrophosphate

R5P: ribose-5-phosphate

RNR: ribonucleotide reductase

ROS: reactive oxygen species

SEM-EDS: scanning electron microscopy with energy-dispersive X-ray spectroscopy

TBHP: Tert-butyl hydroperoxide

α-KG: α-ketoglutarate

Supplementary information

Supplementary Information. Contains Supplementary Figures S1–S9, Supplementary Tables S1–S2 and supplementary references.

Declarations

Ethics approval and consent to participate

Not applicable.

Consent for publication

Not applicable.

Availability of data and materials

The raw LC–MS files and sample metadata generated from the $^{13}C_2$-glutamine tracing experiment, including intracellular extracts and corresponding conditioned-medium samples, have been deposited in Zenodo under the reserved DOI https://doi.org/10.5281/zenodo.21714030. All other data supporting the findings of this study are included in the article and its supplementary information or are available from the corresponding author on reasonable request.

Competing interests

The authors declare that they have no competing interests.

Funding

The authors acknowledge financial support from the European Union's Horizon 2020 research and innovation program under grant agreement No. 857287 (BBCE).

Authors' contributions

J.F. conceived the study, performed the experiments, analyzed and interpreted the data, and wrote the original draft of the manuscript. A.V. performed LC-MS based metabolomics experiment. X.J. performed and analyzed the alkaline comet assay. F. Z. and X. W. contributed to the supervision and editing of the manuscript. K.K. provided funding acquisition, conceptualization, supervision, and revised the manuscript.

Acknowledgements

The authors gratefully acknowledge Prof. Janis Locs (Institute of Biomaterials and Bioengineering, Riga Technical University) for supplying the gallium nitrate utilized in this study.

References

1 Mosina M, Kovrlija I, Stipniece L, Locs J. Gallium containing calcium phosphates: Potential antibacterial agents or fictitious truth. *Acta Biomater* 2022; **150**: 48–57.

2 Minandri F, Bonchi C, Frangipani E, Imperi F, Visca P. Promises and failures of gallium as an antibacterial agent. *Future Microbiol* 2014; **9**: 379–397.

3 Peng XX, Gao S, Zhang JL. Gallium (III) Complexes in Cancer Chemotherapy. *Eur J Inorg Chem* 2022; **2022**: 1–9.

4 Kubista B, Schoefl T, Mayr L, Van Schoonhoven S, Heffeter P, Windhager R *et al.* Distinct activity of the bone-targeted gallium compound KP46 against osteosarcoma cells - Synergism with autophagy inhibition. *Journal of Experimental and Clinical Cancer Research* 2017; **36**: 1–13.

5 Timerbaev AR. Advances in developing tris(8-quinolinolato)gallium(iii) as an anticancer drug: Critical appraisal and prospects. *Metallomics* 2009; **1**: 193–198.

6 Peng XX, Zhang H, Zhang R, Li ZH, Yang ZS, Zhang J *et al.* Gallium Triggers Ferroptosis through a Synergistic Mechanism. *Angew Chem Int Ed* 2023; **515031**. doi:10.1002/anie.202307838.

7 Chen CH, Huang YM, Grillet L, Hsieh YC, Yang YW, Lo KY. Gallium maltolate shows synergism with cisplatin and activates nucleolar stress and ferroptosis in human breast carcinoma cells. *Cellular Oncology* 2023; **46**: 1127–1142.

8 Li W, Yang C, Cheng Z, Wu Y, Zhou S, Qi X *et al.* Gallium complex K6 inhibits colorectal cancer by increasing ROS levels to induce DNA damage and enhance phosphatase and tensin homolog activity. *MedComm (Beijing)* 2024; **5**. doi:10.1002/mco2.665.

9 Qi J, Qian K, Tian L, Cheng Z, Wang Y. Gallium(iii)-2-benzoylpyridine-thiosemicarbazone complexes promote apoptosis through Ca2+ signaling and ROS-mediated mitochondrial pathways. *New Journal of Chemistry* 2018; **42**: 10226–10233.

10 Chang KL, Liao WT, Yu CL, Lan CCE, Chang LW, Yu HS. Effects of gallium on immune stimulation and apoptosis induction in human peripheral blood mononuclear cells. *Toxicol Appl Pharmacol* 2003; **193**: 209–217.

11 Gallego B, Kaluderovic MR, Kommera H, Paschke R, Hey-Hawkins E, Remmerbach TW *et al.* Cytotoxicity, apoptosis and study of the DNA-binding properties of bi- and tetranuclear gallium(III) complexes with heterocyclic thiolato ligands. *Invest New Drugs* 2011; **29**: 932–944.

12 Valiahdi SM, Heffeter P, Jakupec MA, Marculescu R, Berger W, Rappersberger K *et al.* The gallium complex KP46 exerts strong activity against primary explanted melanoma cells and induces apoptosis in melanoma cell lines. *Melanoma Res* 2009; **19**: 283–293.

13 Goss CH, Kaneko Y, Khuu L, Anderson GD, Ravishankar S, Aitken ML *et al.* Gallium disrupts bacterial iron metabolism and has therapeutic effects in mice and humans with lung infections. *Sci Transl Med* 2018; **10**: 1–12.

14 Chitambar CR. Gallium and its competing roles with iron in biological systems. *Biochim Biophys Acta Mol Cell Res* 2016; **1863**: 2044–2053.

15 Yang M, Chitambar CR. Role of oxidative stress in the induction of metallothionein-2A and heme oxygenase-1 gene expression by the antineoplastic agent gallium nitrate in human lymphoma cells. *Free Radic Biol Med* 2008; **45**: 763–772.

16 Chitambar CR. Medical applications and toxicities of gallium compounds. *Int J Environ Res Public Health* 2010; **7**: 2337–2361.

17 Arafeh R, Shibue T, Dempster JM, Hahn WC, Vazquez F. The present and future of the Cancer Dependency Map. *Nat Rev Cancer* 2025; **25**: 59–73.

18 Meng EC, Goddard TD, Pettersen EF, Couch GS, Pearson ZJ, Morris JH *et al.* UCSF ChimeraX: Tools for structure building and analysis. *Protein Science* 2023; **32**. doi:10.1002/pro.4792.

19 Kurtuldu F, Mutlu N, Boccaccini AR, Galusek D. Gallium containing bioactive materials: A review of anticancer, antibacterial, and osteogenic properties. *Bioact Mater* 2022; **17**: 125–146.

20 Li F, Liu F, Huang K, Yang S. Advancement of Gallium and Gallium-Based Compounds as Antimicrobial Agents. *Front Bioeng Biotechnol* 2022; **10**: 1–15.

21 Bernstein LR, Park M. Gallium, Therapeutic Effects. *Encyclopedia of Metalloproteins* 2013. doi:10.1007/978-1-4614-1533-6.

22 Sun W, Qi M, Cheng S, Li C, Dong B, Wang L. Gallium and gallium compounds: New insights into the “Trojan horse” strategy in medical applications. *Mater Des* 2023; **227**: 111704.

23 Lane AN, Fan TWM. Regulation of mammalian nucleotide metabolism and biosynthesis. Nucleic Acids Res. 2015; **43**: 2466–2485.

24 Popović-Bijelić A, Kowol CR, Lind MES, Luo J, Himo F, Enyedy ÉA *et al.* Ribonucleotide reductase inhibition by metal complexes of Triapine (3-aminopyridine-2-carboxaldehyde thiosemicarbazone): A combined experimental and theoretical study. *J Inorg Biochem* 2011; **105**: 1422–1431.

25 Casey Z, Randall T, Nupur D, Yatrik S, Kathleen S, Christopher C. Ferroportin-dependent iron efflux as a novel mechanism of gallium maltolate in glioblastoma. Neuro-Oncology, Volume 27, Issue Supplement 5, 2025, Pages v176–v177.

26 Fan J, Schiemer T, Vaska A, Jahed V, Klavins K. Cell via Cell Viability Assay Changes Cellular Metabolic Characteristics by Intervening with Glycolysis and Pentose Phosphate Pathway. *Chem Res Toxicol* 2024; **37**: 208–211.

27 Pang Z, Zhou G, Ewald J, Chang L, Hacariz O, Basu N *et al.* Using MetaboAnalyst 5.0 for LC–HRMS spectra processing, multi-omics integration and covariate adjustment of global metabolomics data. *Nat Protoc* 2022; **17**: 1735–1761.

Supplementary Files

This is a list of supplementary files associated with this preprint. Click to download.

- sourcedata.xlsx
- GalliumSupplementaryInformation.docx